

Visualizing p -orbital texture in the charge-density-wave state of CeSbTe

Xinglu Que¹, Qingyu He¹, Lihui Zhou¹, Shiming Lei^{2,a}, Leslie Schoop², Dennis Huang^{1,*}, and Hidenori Takagi^{1,3,4}

1. Max Planck Institute for Solid State Research, Heisenbergstr. 1, 70569 Stuttgart, Germany

2. Department of Chemistry, Princeton University, Princeton, NJ 08544, USA

3. Institute for Functional Matter and Quantum Technologies, University of Stuttgart, 70569 Stuttgart, Germany

4. Department of Physics, University of Tokyo, 113-0033 Tokyo, Japan

a. Present address: Department of Physics, Hong Kong University of Science and Technology, Clear Water Bay, Hong Kong, China

*Corresponding author: D.Huang@fkf.mpg.de

The collective reorganization of electrons into a charge density wave (CDW) inside a crystal has long served as a textbook example of an ordered phase in condensed matter physics. Two-dimensional square lattices with p electrons are well-suited to the realization of CDW, due to the anisotropy of the p orbitals and the resulting one dimensionality of the electronic structure. In spite of a long history of study of CDW in square-lattice systems, few reports have recognized the existence and significance of a hidden orbital degree of freedom. The degeneracy of p_x and p_y electrons inherent to a square lattice may give rise to nontrivial orbital patterns in real space that endow the CDW with additional broken symmetries or unusual order parameters. Using scanning tunneling microscopy, we visualize signatures of p -orbital texture in the CDW state of the topological semimetal candidate CeSbTe, which contains Sb square lattices with $5p$ electrons. We image atomic-sized, anisotropic lobes of charge density with periodically modulating anisotropy, that ultimately can be mapped onto a microscopic pattern of p_x and p_y bond density waves. Our results show that even delocalized p orbitals can reorganize into unexpected and emergent electronic states of matter.

Main

The p -electron square lattice represents a prototypical model for charge density wave (CDW) in two dimensions (2D) (1-4). As shown in Fig. 1a, we consider degenerate, half-filled $p_{x'}$ and $p_{y'}$ orbitals, where the (x', y') axes are defined along the nearest-neighbor bonds with length a' . Due to the anisotropy of the p orbitals, σ hopping is much larger than π hopping, leading $p_{x'}$ electrons to propagate predominantly along the x' direction and $p_{y'}$ electrons to propagate predominantly along the y' direction. This anisotropy is reflected in the Fermi surface, which comprises quasi-1D $p_{x'}$ bands centered around crystal momentum $k_{x'} = \pm\pi/(2a')$ and quasi-1D $p_{y'}$ bands centered around $k_{y'} = \pm\pi/(2a')$.

In the limit of only σ hopping, t_σ , the $p_{x'}$ and $p_{y'}$ bands are fully 1D and we can consider a few possible CDW states with different wave vectors (Fig. 1b). A wave vector $\mathbf{q} = (\pi/a', 0)$ nests the $p_{x'}$ bands and corresponds in real space to a bond density wave of $p_{x'}$ electrons with periodicity $2a'$ along the x' axis (Fig. 1c). This bond density wave can be viewed as parallel chains of dimerized $p_{x'}$ orbitals with σ overlap and is analogous to the Peierls distortion of a 1D chain of s orbitals. Equivalently, a wave vector $\mathbf{q} = (0, \pi/a')$ nests the $p_{y'}$ bands and gives rise to a bond density wave of $p_{y'}$ electrons with periodicity $2a'$ along the y' axis (Fig. 1d). Another wave vector $\mathbf{q} = (\pi/a', \pi/a')$ simultaneously nests both the $p_{x'}$ and $p_{y'}$ bands. In real space, the corresponding CDW state is one where the neighboring chains of dimerized $p_{x'}$ and $p_{y'}$ orbitals are phase-shifted by a' relative to one another, resulting in a $\sqrt{2}a' \times \sqrt{2}a'$ supercell rotated by 45° relative to the primitive unit cell (Fig. 1e). The phase shift incurs no additional energy cost, as neighboring chains of dimers are independent in the 1D limit we consider, and instead facilitates additional energy gain by allowing the $p_{x'}$ and $p_{y'}$ bands to be simultaneously gapped with a single \mathbf{q} .

An overlooked feature of this textbook model is the underlying orbital degree of freedom. In the case of the $\mathbf{q} = (\pi/a', \pi/a')$ CDW state, we essentially have independent $p_{x'}$ and $p_{y'}$ bond density waves, and the degree of freedom concerns how these two should be superimposed in real space. One such superposition results in extended zigzag bonds of p orbitals that run along the $[11]$ direction (Fig. 1f). Another such superposition with a different phase relationship between the two density waves results in extended zigzag bonds that run along the $[\bar{1}1]$ direction. Here, the two possible superpositions are trivially related by a 90° rotation. If we have $p_{x'}$ and $p_{y'}$ bond density waves with longer wavelengths and more complicated patterns, superimposing the two density waves with different phase relationships may result in actually distinct patterns. In reality, the dimerized chains of $p_{x'}$ and $p_{y'}$ orbitals are not fully independent, but interact via interchain hopping (t_π) and interorbital hopping (t' ; see Fig. 1a), which then select the real-space structure and relative phase of $p_{x'}$ and $p_{y'}$ bonds within the CDW state. Exotic phases with spatially varying p -orbital texture in 2D have been discussed in the context of optical lattices of ultracold atoms (5-8), but their realization and visualization in solid-state crystals with valence p electrons remain rare.

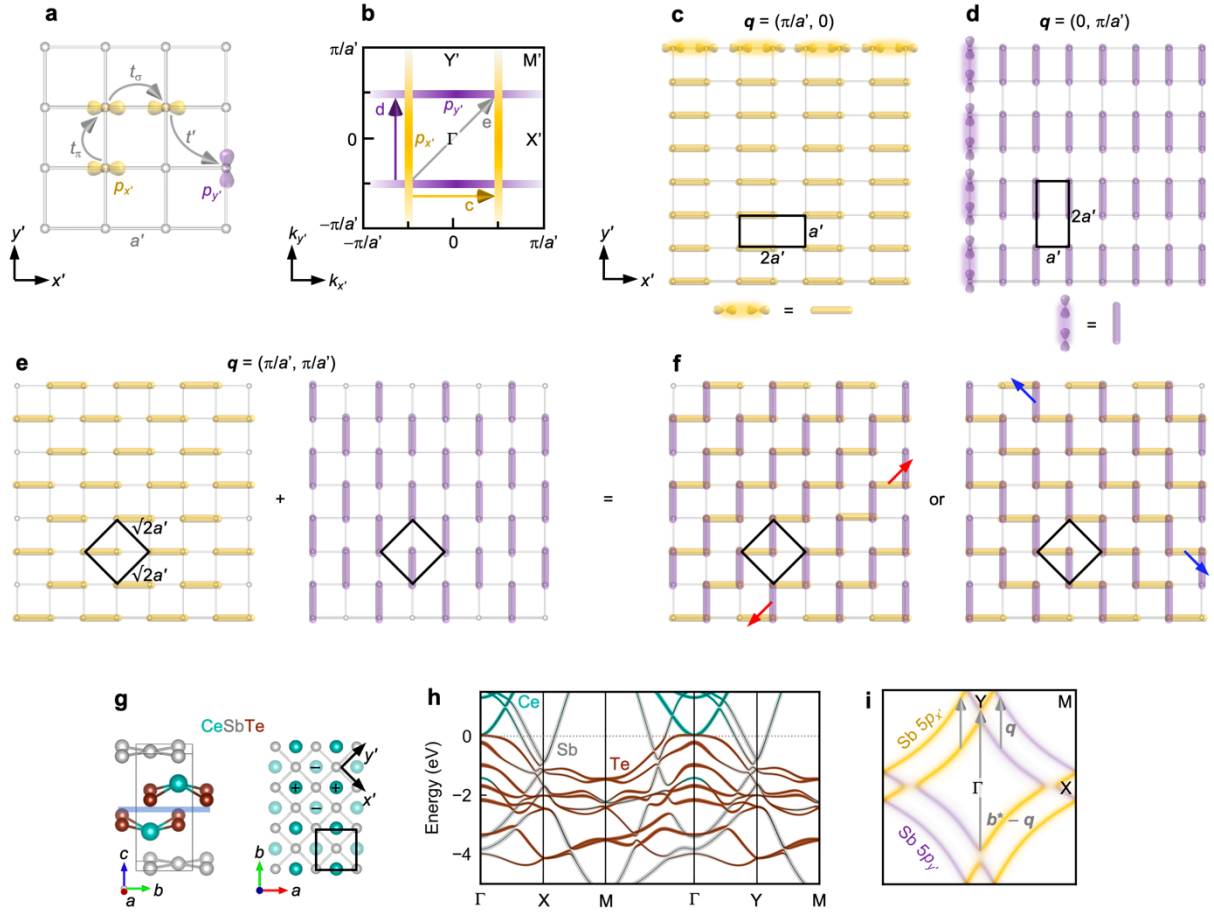


Fig. 1: p -electron phases on a square lattice and CeSbTe. **a**, Tight-binding model of p_x and p_y electrons on a square lattice with bond length a' and hopping parameters t_σ , t_π , and t' . The axes (x', y') are defined along the bond directions of the square lattice. **b**, Schematic Fermi surface in the limit of $t_\sigma \gg t_\pi \sim t' \sim 0$. Yellow (purple) denotes the contribution from p_x (p_y) orbitals. **c**, Bond density wave of p_x electrons with wave vector $\mathbf{q} = (\pi/a', 0)$, shown as a yellow arrow in **b**. The supercell is enclosed in a black box. **d**, Bond density wave of p_y electrons with wave vector $\mathbf{q} = (0, \pi/a')$, shown as a purple arrow in **b**. **e**, The wave vector $\mathbf{q} = (\pi/a', \pi/a')$ simultaneously nests both p_x and p_y Fermi sheets (gray arrow in **b**) and results in both p_x and p_y bond density waves. **f**, The superposition of p_x and p_y bond density waves results in zigzag bond patterns that extend either along the $[11]$ or $[\bar{1}1]$ directions, depending on the relative phase of the two density waves. **g**, Crystal structure of CeSbTe. The (a, b) axes are rotated 45° from the (x', y') axes. The blue plane indicates where cleavage takes place between two CeTe layers. The Ce atoms labeled (+) and (-) lie above and below the Sb square lattice, respectively, which enlarges the unit cell to contain two Sb atoms. **h**, Calculated band structure of Ce(Sb $_{1-x}$ Te $_x$)Te decomposed into corresponding contributions from Ce, Sb, and Te. The virtual crystal approximation was applied to simulate a Te substitutional level of $x = 0.37$ (see Methods for details of calculations and Supplementary Note 2 for estimation of doping level). **i**, Tight-binding approximation of the Fermi surface with p -orbital characters and CDW wave vectors shown.

$R\text{Te}_3$, $R\text{Te}_2$, and $RSb\text{Te}$ (R = rare earth element) are related material classes that host 2D square lattices of pnictogen or chalcogen atoms with p electrons sandwiched by (generally) magnetic buffer layers. While the study of CDW in these materials has an extensive history (1, 9-16), only recently have any experimental signatures emerged indicating a nontrivial orbital texture in the CDW state. Raman

spectroscopy measurements probing the collective amplitude mode of the CDW in GdTe_3 and LaTe_3 detected an unexpected axial symmetry (17), which points to an unconventional order parameter for the CDW, possibly with finite orbital angular momentum (18, 19). The microscopic orbital pattern that is inferred to be responsible for this state, however, has not yet been directly imaged.

We focus on CeSbTe (20), which has drawn renewed interest as a material platform that offers Dirac-like bands tunable by magnetism and CDW (21, 22). The compound is composed of Sb square lattices separated by CeTe layers (Fig. 1g). Due to the staggered arrangement of Ce atoms above and below the Sb plane, the Sb square lattice acquires nonsymmorphic symmetry and has doubled in-plane periodicity, with two Sb atoms per unit cell. The folding of the Sb 5*p* bands creates linearly dispersing bands with an approximate Dirac line node near the Fermi energy, whose diamond shape reflects the quasi-1D nature of p_x and p_y electrons we discussed (23, 24) (see Supplementary Note 1 for a tight-binding analysis). Various band crossings can be split and shifted when the magnetic moments of Ce^{3+} order antiferromagnetically below 2.7 K or ferromagnetically in an external magnetic field (21). Stoichiometric CeSbTe is difficult to synthesize, as Te atoms (x) tend to replace Sb atoms in the square lattice, or leave behind vacancies (δ) in the CeTe layers, as represented by the formula $\text{Ce}(\text{Sb}_{1-x}\text{Te}_x)\text{Te}_{1-\delta}$. With increasing x , additional electrons are doped into the Sb square lattice. The Dirac node sinks below the Fermi energy (E_F) (Fig. 1h) and the Fermi surface arising from the Sb 5*p* orbitals splits into two concentric, diamond-shaped sheets (Fig. 1i). CDW states appear with $1 \times 5 \times 1$, $1 \times 3 \times 1$, and $3 \times 3 \times 2$ superstructures around x values of 0.49, 0.66, and 0.89, respectively (22, 25). The increase of the CDW wave vector with increasing x suggests that it is related to the nesting wave vector of the double-diamond Fermi surface, which also grows with increasing x (arrows in Fig. 1i). X-ray diffraction has revealed that in these CDW phases, the Sb-Sb bond lengths show the greatest disproportionation and the Sb square lattice distorts into various bonding patterns (22). The question remains as to how the electronic orbitals organize in these states.

Here, we used scanning tunneling microscopy (STM) to perform real-space imaging of a 1×7 CDW state in a $\text{Ce}(\text{Sb}_{1-x}\text{Te}_x)\text{Te}_{1-\delta}$ crystal with estimated $x \sim 0.39$ and $\delta \sim 0.04$ (see Supplementary Note 3 for an estimate of the Te vacancy concentration). As an atomically-resolved tool, STM enabled us to elucidate the internal CDW structure with a high level of detail. Although the CDW originates predominantly from the Sb square lattice two atomic planes below the cleaved Te surface, by using an appropriate tunneling bias voltage where the Te partial density of states (DOS) is suppressed, we could image electronic contributions from the subsurface Sb 5*p* orbitals. The constant-current topography reveals a complex state of atomic-sized lobes of charge density with spatial distribution spreading close to and along Sb-Sb bonds. The lobes are anisotropic and their axis of anisotropy varies periodically in space, alternating between the crystalline a and b axes. We map this pattern onto a superposition of Sb 5*p_x* and 5*p_y* bond density waves that are identical in structure, but shifted in phase relative to each other. The p_x and p_y bond density waves are essentially building blocks whose superposition can give rise to

CDWs with nontrivial orbital patterns. Our measurements demonstrate that *RSbTe* and related compounds are not only platforms for magnetic topological bands, as frequently discussed, but also hosts to spatially modulated *p*-electron phases.

STM imaging of CDW on surface

We performed STM imaging of cleaved single crystals of $\text{Ce}(\text{Sb}_{1-x}\text{Te}_x)\text{Te}_{1-\delta}$ at a temperature of 4.2 K and a magnetic field of 0 T, which lie in the paramagnetic phase of *CeSbTe* (see [Supplementary Note 4 for the magnetic phase diagram](#)). Figure 2a presents a typical STM topography acquired with a negative sample-tip bias voltage of -0.5 V, which involves tunneling from the filled orbitals of the sample. The image reveals a square lattice of isotropic lobes with an average distance of 4.14 Å, as extracted from the Fourier transform (FT) (Fig. 2b). The lattice constant immediately excludes the Sb square lattice with Sb-Sb distance of 3.08 Å as the origin of the observed lattice of bright lobes, but is consistent with either the Ce or Te sublattices of the *CeTe* buffer layer with Ce-Ce and Te-Te distances of 4.35 Å. Since the weakest bonds in the crystal lie between two adjacent Te planes (shaded plane in Fig. 1g), the surface termination is mostly likely a Te plane. This identification is corroborated by the sizeable number of vacancies $\sim 4\%$, as expected for Te in $\text{Ce}(\text{Sb}_{1-x}\text{Te}_x)\text{Te}_{1-\delta}$ (see inset of Fig. 2a for a higher resolution image). We did not observe any other kinds of surface terminations.

In addition to the atomically resolved Te lattice, we spotted a unidirectional CDW running parallel to the Te-Te bond directions, i.e., the direction of the nesting wave vectors shown in Fig. 1i. In Fig. 2a, the CDW appears as a weak amplitude modulation superimposed on the atomic corrugations. The CDW is better visualized in an autocorrelation of the topography (Fig. 2c), which reveals an amplitude modulation of length a that corresponds to the atomic lattice, plus a longer amplitude modulation of length $\sim 7a$ that corresponds to the CDW (see line cut in Fig. 2c). The CDW is also observable as superstructure peaks in the FT (Fig. 2b), from which we extract the actual CDW wavelength in the field of view to be $6.85a$, which is slightly smaller than $7a$, likely due to local discommensurations. By analyzing over 30 topographic images, we determine the average CDW wavelength to be $6.9 \pm 0.4a$ for the $\text{Ce}(\text{Sb}_{1-x}\text{Te}_x)\text{Te}_{1-\delta}$ sample presented here in the main text (see [Supplementary Note 3 for statistics](#)).

Figure 2d presents another negative-bias topography acquired over a larger field of view of 90×200 nm. We observed four domains, two with CDW along the horizontal axis of the image, and the other two with CDW along the vertical axis of the image. The domains range from roughly 30 to 100 nm in width. The 90° rotation of the CDW modulation can be directly seen, but is also confirmed by FTs of selected areas within single domains (Fig. 2e). The observation of rotated domains helps exclude tip artifacts as the source of the unidirectional 1×7 CDW. At the boundary between domains, the overlap region between orthogonal CDWs is roughly two to three CDW periods, as seen in the Fourier-filtered

image of Fig. 2f. The CDW is relatively local in character and thereby reasonably robust against disorder.

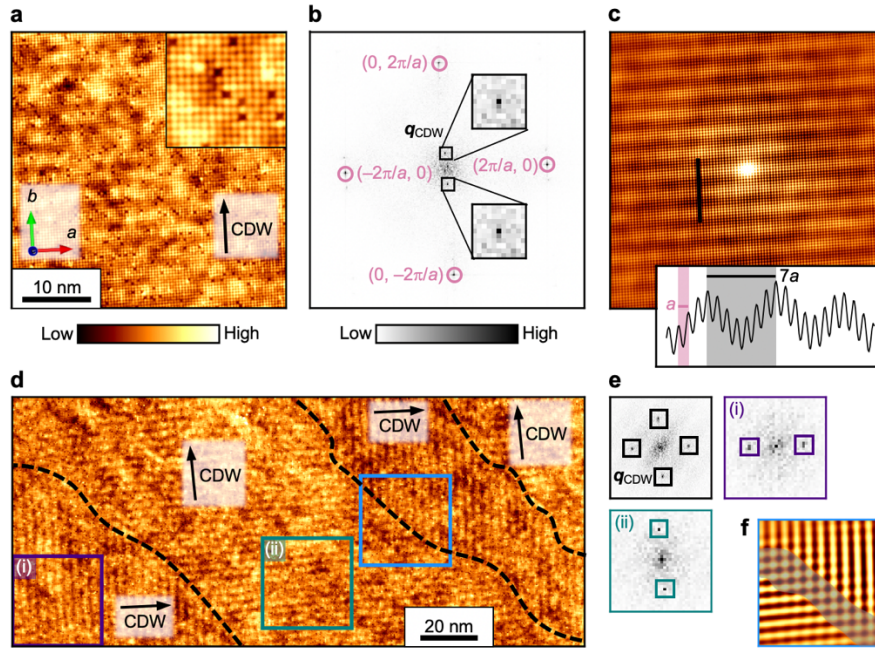


Fig. 2: STM imaging of unidirectional CDW on the Te-terminated surface. **a**, Typical topographic image measured by STM with CDW direction marked by the black arrow. Inset: high-resolution topography of a smaller 4.1×4.1 nm area, illustrating atomic resolution. Setpoint: -0.5 V, 80 pA. **b**, Fourier transform (FT) of the area shown in **a**. The Bragg peaks q_{Bragg} and CDW peaks $q_{\text{CDW}} \sim 1/7 q_{\text{Bragg}}$ are enclosed in the pink circles and black squares, respectively. **c**, Autocorrelation of **a**. The inset shows a height profile corresponding to the black line cut. **d**, Topography of a larger field of view, revealing domains of orthogonal unidirectional CDW with directions marked by the black arrows. The domain boundaries are indicated by the dashed black lines. Setpoint: -0.5 V, 80 pA. **e**, FTs of the entire field of view in **d** (upper left panel) and of restricted areas (i) and (ii) (upper right and lower left panels). **f**, Blue boxed region in **d** with Fourier filtering around the CDW peaks, illustrating a narrow boundary region between domains where the CDW appears bidirectional (shaded region).

STM imaging of CDW internal structure below surface

The STM topography appears drastically different when measured at positive sample-tip bias voltages; i.e., via tunneling into the empty orbitals of the sample. Figures 3a and 3b compare constant-current topographies simultaneously obtained over the same 20×20 nm area at -0.5 and $+1.0$ V (see [Methods for explanation of Multi Pass imaging mode](#)). Their corresponding FTs are shown in Figs. 3c and 3d. In the -0.5 V topography, the aforementioned 1×7 background modulation is barely visible by eye, and is better detected in the FT as weak CDW satellite peaks. In the $+1.0$ V topography, the 1×7 pattern becomes strongly manifested, but with a complicated internal structure, rather than just a simple modulation of amplitude. Further contrasts between -0.5 and $+1.0$ V imaging are highlighted by inspecting the enlarged views of the two topographies in Figs. 3e and 3f. The -0.5 V topography consists of atomic-sized lobes of charge density that are isotropic in shape (dashed circles in Fig. 3e). The

positions of the lobes, which we identify by extracting the positions of all the local maxima in the topography (dots in Fig. 3e), form a mostly square lattice, with occasional vacancies and dislocations. On the other hand, the +1.0 V topography shows atomic-sized lobes that are anisotropic and elongated along either the x or y directions (red and blue dashed ellipses in Fig. 3f), which correspond to the crystallographic b and a axes. Their spatial distributions are shifted relative to the positions of the isotropic lobes seen at -0.5 V (gray dots in Fig. 3f) and also distorted from a regular square lattice. In the remainder of the paper, we focus on the analysis and interpretation of these unusual features in the +1.0 V image.

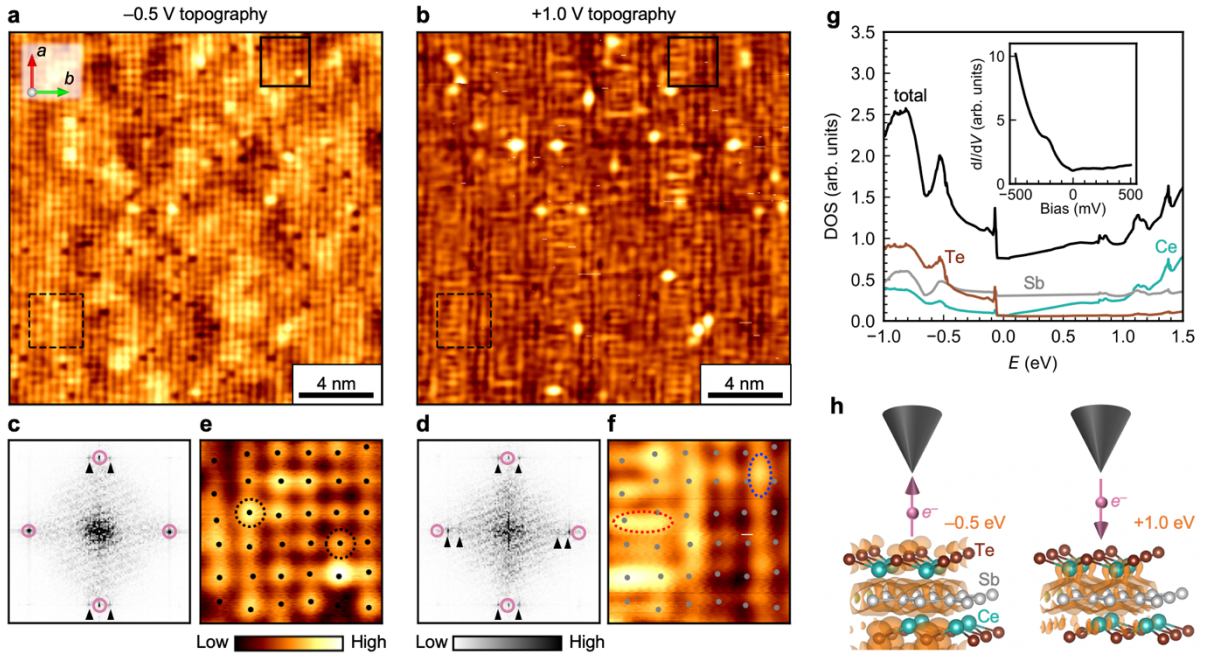


Fig. 3: Layer-resolved imaging by varying bias voltage. **a** and **b**, STM topographies of the same 20×20 nm field of view imaged with -0.5 and $+1.0$ V biases, respectively. Setpoint current: 20 pA. **c** and **d**, FTs of **a** and **b**, respectively. Bragg and CDW satellite peaks are marked by pink circles and black triangles, respectively. **e** and **f**, Enlarged view of the solid boxed regions in **a** and **b**, respectively. The dashed circles and ellipses highlight the shapes of the charge density lobes. The black dots in **e** indicate points of local maxima in the topography. The gray dots in **f** are the positions of the local maxima in **e** superimposed. **g**, DFT-computed total and atomically resolved DOS of $\text{CeSb}_{0.63}\text{Te}_{1.37}$. The inset is a dI/dV spectrum measured via STM. Setup conditions: -0.5 V, 100 pA. **h**, DFT-computed isosurfaces of partial charge density, illustrating the orbitals involved in the tunneling processes of a Te-terminated surface. The partial charge density on the left includes states between $0 (=E_F)$ to -0.5 eV, matching the -0.5 V topography in **a**, while the partial charge density on the right includes states between 0 and $+1.0$ eV, matching the $+1.0$ V topography in **b**.

Insights as to why the +1.0 V image appears so distinct can be gleaned from density functional theory (DFT) calculations (see [Methods for details of DFT calculations](#)). The computed DOS reproduces the asymmetric V-shaped dI/dV measured by STM (Fig. 3g). The DOS consists of Sb contributions that are nearly constant as a function of energy, Ce contributions that show a V-shaped depression centered

at E_F , and Te contributions that are large below E_F , but nearly zero above E_F . The schematics in Fig. 3h depict the integrated partial charge densities for a Te-terminated slab corresponding to -0.5 and $+1.0$ V STM constant-current imaging. When imaging at -0.5 V, electrons tunnel from occupied surface Te p_z orbitals into the tip, so the isotropic lobes arranged on a square lattice in Fig. 3e can be identified with Te atoms. The weakness of the observed CDW amplitude here may be expected, as the CDW-active Sb layer, which shows the largest periodic lattice distortions (26), is not involved. When imaging at $+1.0$ V, electrons tunnel from the tip into unoccupied orbitals of the surface, but since there are nearly no available Te orbitals, the electrons tunnel deeper into subsurface Ce $d_{x^2-y^2}$ and Sb p_x and p_y orbitals. The anisotropic shape of the atomic-sized lobes in Fig. 3f suggests contributions from these anisotropic orbitals, and their spatial distributions are indeed shifted laterally from the Te atomic positions. Since the Sb orbitals are involved, the internal texture of the 1×7 CDW state becomes resolvable.

Elucidation of CDW internal structure

The $+1.0$ V topography visibly reveals that the anisotropic lobes of charge density are organized into an intricate pattern. There appears to be a 1×7 periodic alternation between anisotropic lobes elongated along the x direction and anisotropic lobes elongated along the y direction, forming a ladder-like motif with horizontal “rungs” and vertical “rails.” We performed a few steps of analyses to further elucidate the intrinsic underlying structure. First, we used the simultaneously acquired -0.5 V topography of Fig. 3a to construct a reference CeSbTe lattice. We applied Fourier filtering around the Bragg peaks (pink circles in Fig. 3c) to enhance the regularity of the square lattice (Fig. 4a). (See Supplementary Note 5 for the masks used in Fourier filtering.) The positions of the local maxima extracted from this filtered -0.5 V topography represent Te atomic positions (depicted as brown open circles in Figs. 4a and 4b), from which we could also interpolate the Sb-Sb bonds (gray lines in Fig. 4b) and Ce atomic positions (teal dots in Fig. 4b). Second, we extracted the positions of the local maxima of the anisotropic lobes in the $+1.0$ V topography (black dots in Fig. 4c) and placed their coordinates over the reference CeSbTe lattice (Fig. 4d). Although the anisotropic lobes are spatially extended objects, for the purpose of analysis, we indexed their positions according to their local maxima. Third, we characterized the x or y anisotropy of these lobes as follows: Within the topography $z(x, y)$, we computed and compared the magnitudes of the second partial derivatives $\frac{\partial^2 z}{\partial x^2}$ and $\frac{\partial^2 z}{\partial y^2}$ evaluated at the local maxima (x_i, y_i) of every anisotropic lobe. If $\left| \frac{\partial^2 z}{\partial x^2}(x_i, y_i) \right| < \left| \frac{\partial^2 z}{\partial y^2}(x_i, y_i) \right|$, then the local curvature of the topography is smaller along x than along y , meaning that the anisotropic lobe is elongated more along x than along y . If $\left| \frac{\partial^2 z}{\partial y^2}(x_i, y_i) \right| < \left| \frac{\partial^2 z}{\partial x^2}(x_i, y_i) \right|$, then the anisotropic lobe is elongated more along y than along x . We quantified the degree of anisotropy as

$$\eta(x_i, y_i) = \left| \frac{\partial^2 z}{\partial x^2}(x_i, y_i) \right| - \left| \frac{\partial^2 z}{\partial y^2}(x_i, y_i) \right| - \left(\left| \frac{\partial^2 z}{\partial x^2}(x, y) \right|_{av} - \left| \frac{\partial^2 z}{\partial y^2}(x, y) \right|_{av} \right), \quad (1)$$

where $\left| \frac{\partial^2 z}{\partial x^2}(x_i, y_i) \right|$ is the magnitude of the second partial derivative evaluated at a lobe maximum (x_i, y_i) and $\left| \frac{\partial^2 z}{\partial x^2}(x, y) \right|_{av}$ is the average of the magnitudes of the second partial derivatives computed for all pixels in the field of view. The subtraction of the constant term $\left(\left| \frac{\partial^2 z}{\partial x^2}(x, y) \right|_{av} - \left| \frac{\partial^2 z}{\partial y^2}(x, y) \right|_{av} \right)$ in Eq. (1) accounts for any small global anisotropy that may originate from an imperfect tip. In Fig. 4d, the sign of $\eta(x_i, y_i)$ is represented by the orientation of the rectangles, horizontal for $\eta(x_i, y_i) > 0$ and vertical for $\eta(x_i, y_i) < 0$. The value of $\eta(x_i, y_i)$ is represented by the red-blue color scale, stronger red for increasing x anisotropy and stronger blue for increasing y anisotropy.

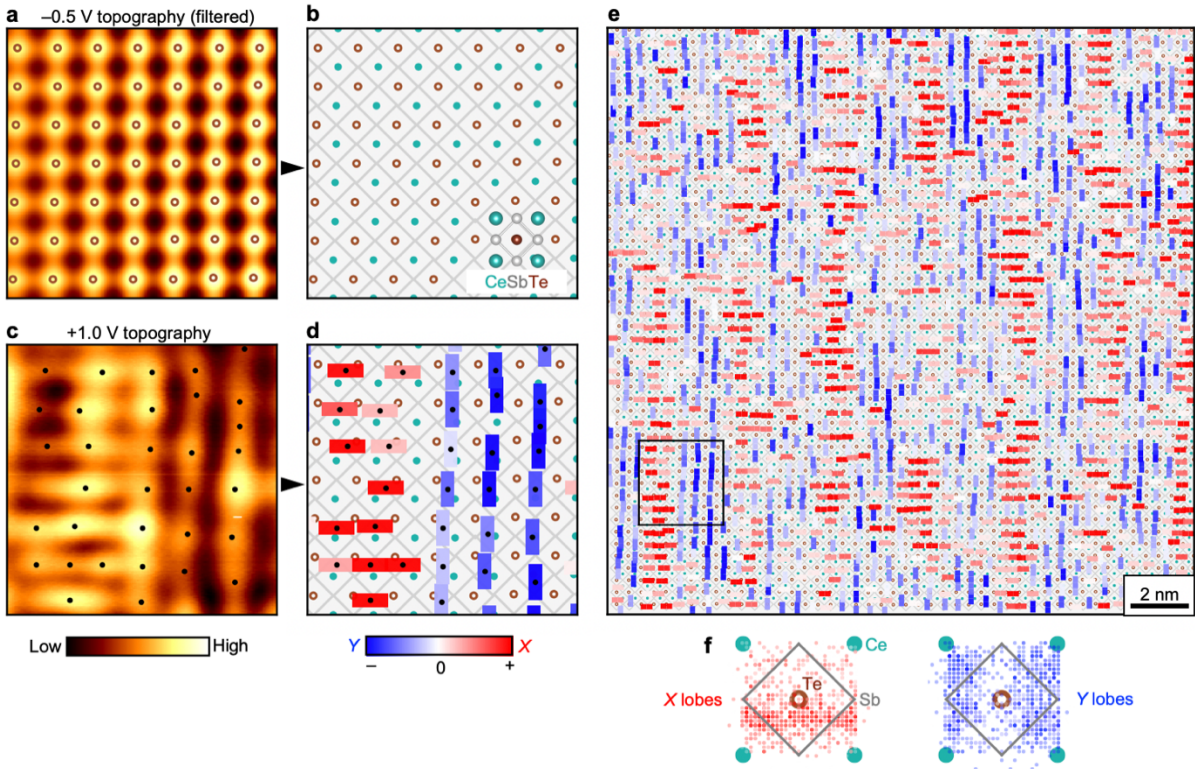


Fig. 4: Visualizing the internal structure of CDW (I): Map of anisotropic lobes. **a**, Selected region of the -0.5 V topography of Fig. 3a with Fourier filtering around the Bragg peaks. The brown open circles indicate the positions of the local maxima, i.e., the Te atomic positions. **b**, Reference CeSbTe lattice extracted from **a**, with Ce represented as teal dots and Sb-Sb bonds as diagonal gray lines. **c**, Same region as **a**, extracted from the $+1.0$ V topography of Fig. 3b. The black dots indicate the positions of the local maxima. **d**, Overlay of anisotropic lobes on the reference CeSbTe lattice. The anisotropic lobes are schematically depicted as rectangles with orientation along x or y . Their colors indicate the degree of lobe anisotropy, as quantified by $\eta(x_i, y_i)$ in Eq. (1). **e**, Map of lobe anisotropy for the entire field of view of Fig. 3b. The black square encloses the selected region shown in **a–d**. (This region is also indicated in Figs. 3a and 3b by the dashed black squares). **f**, Distribution of the positions of the x - and y -anisotropic lobes from **e** within a reference CeSbTe unit cell. The intensity of the red or blue color is proportional to the number of anisotropic lobes at the given position.

Figure 4e presents a composite image that encapsulates the underlying internal structure of the 1×7 CDW state seen in the +1.0 V topography. The anisotropic lobes are represented as horizontal red or vertical blue rectangles according to their x - or y -oriented anisotropy, and the reference CeSbTe unit cells are schematically included. The aforementioned ladder-like motif is clearly evident as periodically alternating striped regions of red and blue rectangles. Less obvious by eye in Fig. 4e is whether there is any pattern or trend for the positions of the red and blue rectangles. By computing 2D histograms in Fig. 4f of the positions of all the anisotropic lobes, we reveal that the x - and y -oriented lobes exhibit distinct spatial distributions within the CeSbTe unit cell. The positions of the x -anisotropic lobes show large scatter along the x axis, but are more confined along the y axis. Their y coordinates are clustered around the lower half of a Te-centered unit cell, just below the Te atom. The positions of the y -anisotropic lobes show, on the contrary, larger scatter along the y axis, but are more confined along the x axis. Their x coordinates are bimodally distributed toward the left and right sides of the Te-centered unit cell. (See Supplementary Note 6 for additional topographies revealing the same internal CDW structure.)

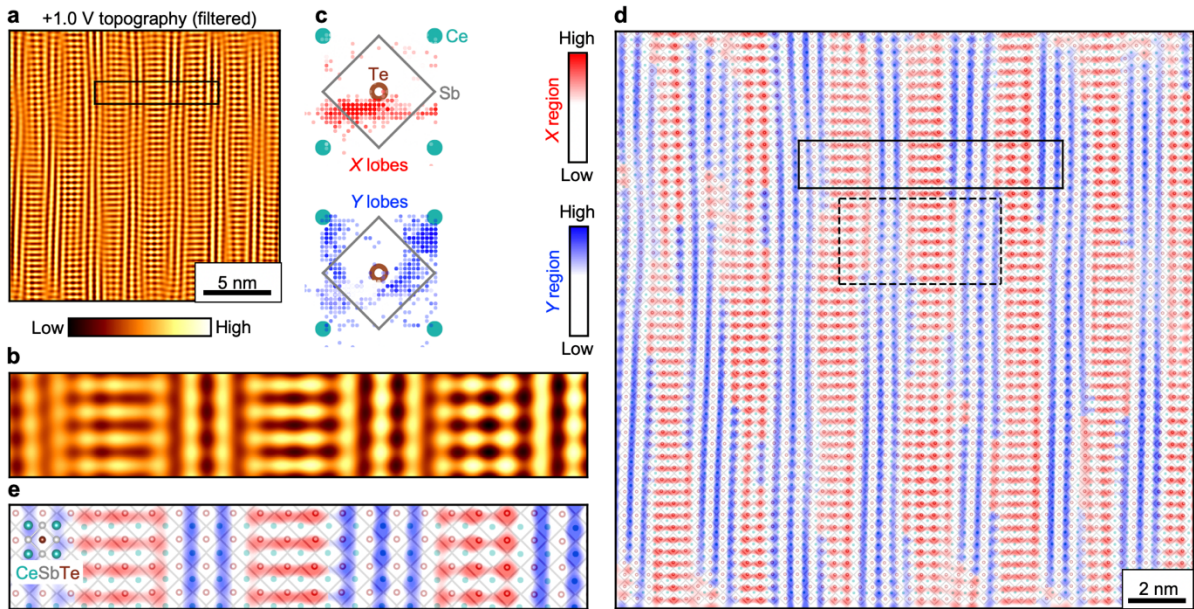


Fig. 5: Visualizing the internal structure of CDW (II): Fourier-filtered pattern. **a** +1.0 V topography of Fig. 3b with Fourier filtering around the Bragg and CDW satellite peaks. **b**, Enlarged view of the boxed region in **a**. **c**, Distribution of the positions of the x - and y -anisotropic lobes within a reference CeSbTe unit cell after applying the Fourier filtering in **a**. Filtered topography of **a** with red-blue binning applied to demarcate regions of predominant x (red) or y (blue) anisotropy. The Ce, Sb, and Te atomic positions are included. **e**, Enlarged view of the solid boxed region in **d**.

The analyses that culminate in Figs. 4e and 4f capture the essential internal features of the 1×7 CDW state in CeSbTe. A sizable level of disorder, likely due to Te substitutions in the subsurface Sb layer, is nevertheless still present in these images. On one hand, STM is well-suited to resolve the local impact of defects on CDW. On the other hand, to enhance our visualization of the intrinsic CDW pattern, we additionally performed Fourier filtering of the +1.0 V topography around the Bragg and CDW

satellite peaks (pink circles and black triangles in Fig. 3d). The resulting topography in Fig. 5a manifests the ladder-like motif much more clearly. Three periods of such “ladders” are shown in Fig. 5b. Repeating the same analyses of Fig. 4 with this filtered topography, we find the scatter in the positions of the x - and y -anisotropic lobes within the CeSbTe unit cell to be much reduced. The coordinates of the x -anisotropic lobes spread somewhere between the Te atom and the two Sb-Sb bonds in the lower half of the Te-centered unit cell. The coordinates of the y -anisotropic lobes show a sharper bimodal distribution towards the left and right sides of the Te-centered unit cell compared to that in Fig. 4f and appear to cluster around Sb-Sb bonds and the Ce atoms. This spatial arrangement of anisotropic lobes is also visible locally within a CDW period, as seen in Figs. 5d and 5e. In Fig. 5d, we binned the filtered +1.0 V topography into red or blue regions according to the predominant x or y orientation of the anisotropic lobes. Figure 5e shows the enlarged view of a small region. The anisotropic lobes look like they overlap with Sb-Sb bonds forming zigzag patterns that extend either along the crystallographic a or b directions, which is reminiscent of the pictures presented in Fig. 1f.

Microscopic picture

Before we can connect our STM image to a model of $p_{x'}$ and $p_{y'}$ bond density waves, we need to consider one additional factor. Since we require large positive biases to tunnel through the surface Te atoms, we are likely probing unoccupied antibonding states associated with the CDW. We performed DFT calculations of the simpler 1×1 CDW state of CeSbTe to verify this point. The partial charge density integrated from 0 ($=E_F$) to +1.0 eV shows lobes that are directed away from the stronger Sb-Sb bonds and that overlap along the weaker Sb-Sb bonds (Fig. 6a). The local maxima of the anisotropic lobes imaged at +1.0 V should thus be associated with weaker Sb-Sb bonds, while the local minima between the lobes should be associated with the stronger Sb-Sb bonds. In the field of view of Fig. 6b, we extract all the Sb-Sb bonds which lie in the local minima (white regions) between the anisotropic lobes (red and blue regions), which together constitute the underlying pattern of bond density waves. The pattern indeed consists of zigzag chains of Sb-Sb bonds that alternate in extension along the a and b axes.

Figures 6c–6e show a decomposition of the experimentally determined 1×7 CDW structure into a superposition of $p_{x'}$ and $p_{y'}$ bond density waves. While the patterns are highly nontrivial, a closer inspection reveals a fundamental similarity to the $p_{x'}$ and $p_{y'}$ bond density waves of the simpler 1×1 CDW (Fig. 1e). The patterns in Figs. 6d and 6e comprise chains of $p_{x'}$ and $p_{y'}$ orbitals along the x' and y' directions, respectively, that are almost regularly dimerized, and the neighboring chains have a relative phase shift of a' . Along each chain, however, there are periodic phase slips, such as the occurrence of two consecutive strong bonds, i.e., a trimer, or two consecutive weak bonds (examples circled in Fig. 6d). These phase slips effectively enlarge the supercell from 1×1 to 1×7 and distinguish the 1×7 CDW from the 1×1 CDW. Another way to view the existence of phase slips is to consider the nesting wave vector \mathbf{q} subtracted from a reciprocal lattice wave vector \mathbf{b}^* (Fig. 1i). In real space, a wave

vector $\mathbf{b}^* - \mathbf{q}$ implies that the individual $p_{x'}$ and $p_{y'}$ chains should modulate with period $\sim 2.33a'$. These chains should then consist of a majority of $2a'$ dimers, plus periodic phase slips due to the mismatched periodicity of $\sim 2.33a'$.

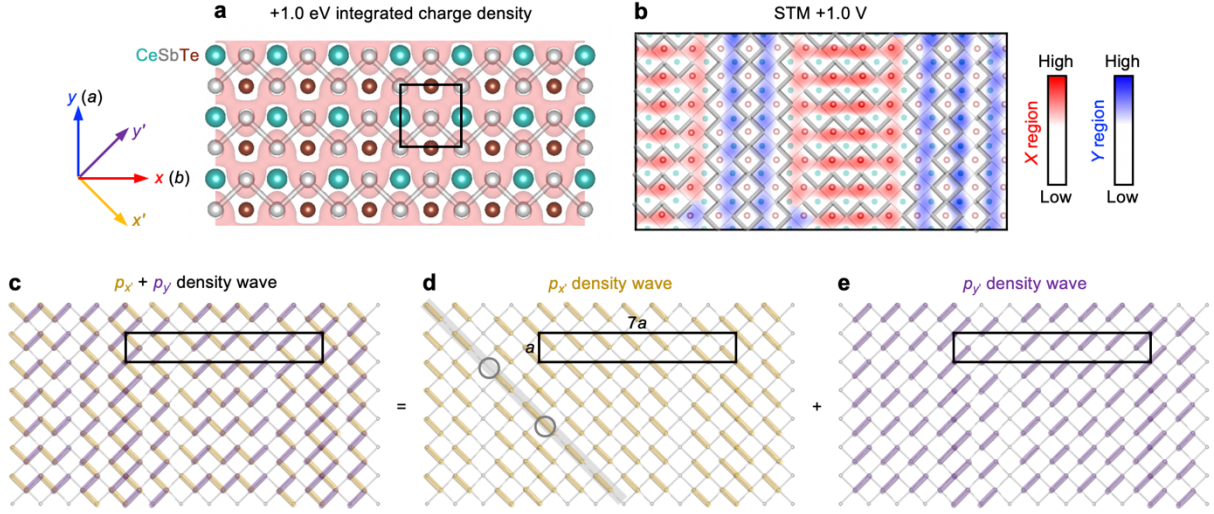


Fig. 6: Bond density wave of Sb $5p_{x'}$ and $5p_{y'}$ orbitals as microscopic origin. **a**, DFT-computed isosurface of partial charge density for a simpler 1×1 CDW state, integrated from 0 ($=E_F$) to +1.0 eV. The lobes of charge density (red shading) are directed away from the stronger Sb-Sb bonds and represent antibonding states. **b**, Filtered STM topography with red-blue binning, reproduced from the dashed boxed region of Fig. 5d. The inferred positions of the stronger Sb-Sb bonds are highlighted with thick gray lines. **c**, Bond density wave pattern of $p_{x'}$ and $p_{y'}$ orbitals with a 1×7 supercell (black rectangle). **d** and **e**, Decomposition of **c** into individual $p_{x'}$ and $p_{y'}$ bond density waves, respectively. The patterns are similar to those of Fig. 1e, except for periodic phase slips (gray circles) that effectively enlarge the CDW supercell to 1×7 .

The key ingredients underlying the 1×7 CDW of CeSbTe and the 1×1 CDW of the square lattice model (Fig. 1) appear to be common. Simultaneous nesting of quasi-1D $p_{x'}$ and $p_{y'}$ Fermi sheets in reciprocal space leads to a superposition of $p_{x'}$ and $p_{y'}$ bond density waves in real space. There is a phase degree of freedom in how these two density waves should be superimposed, which ultimately is fixed by higher-order hopping terms and other additional interactions that hybridize neighboring and intersecting chains of $p_{x'}$ and $p_{y'}$ dimers. In the case of the 1×1 CDW, due to the regular structure of the $p_{x'}$ and $p_{y'}$ dimer chains, we could only obtain a pattern of zigzag bonds that uniformly extend along x or y (Fig. 1f). In the case of the 1×7 CDW, the effective periodicity of the $p_{x'}$ and $p_{y'}$ density waves is enlarged sevenfold by the presence of phase slips that occur along individual chains of $p_{x'}$ or $p_{y'}$ dimers. As a result of these phase slips, more complicated orbital textures can emerge, such as the pattern of alternating x - and y -oriented zigzag bonds that we observed. The CDW in $R\text{Te}_3$ plausibly also involves some superposition of $p_{x'}$ and $p_{y'}$ bond density waves resulting in a nontrivial orbital texture and an amplitude mode with axial symmetry (17, 19).

We note that our microscopic picture considers only the role of Sb $5p$ orbitals. In reality, the x -anisotropic lobes imaged by STM show some spread from the Sb-Sb bonds towards the Te atoms, whereas the y -anisotropic lobes show some spread from the Sb-Sb bonds towards the Ce atoms (Fig. 5c). Based on the +1.0 V tunneling conditions, our image contains convolutions with Ce dx^2-y^2 orbitals and possibly remnant Te p_z orbitals (Figs. 3g and 3h). The role of these additional orbitals in the CDW state remains to be investigated, but they are likely secondary to the Sb $5p$ orbitals.

Outlook

The orbital texture of the CDW on a p -electron square lattice is a consequence of the p_x and p_y orbital degree of freedom inherent to the model. Despite the apparent simplicity of this mechanism, its significance has not been appreciated in $R\text{Te}_3$ until recently (17, 19) and directly imaged in $RSb\text{Te}$ until now. We note that a similar charge-order pattern of alternating anisotropic lobes has been famously imaged in STM experiments of cuprate superconductors (27-30). There, the charge-order period is around $4a$ and orthogonal domains coexist on the scale of several nanometers, giving rise to a charge order that appears more bidirectional (“checkerboard”) in nature. Nevertheless, the anisotropic lobes are spatially arranged with the same ladder-like motif. They are ascribed to O $2p_x$ and $2p_y$ orbitals in the CuO_2 plane that modulate out of phase with each other, endowing the charge order with a d -symmetric form factor (29-31). There are some fundamental differences, however, between the cuprates and $RSb\text{Te}$. In the cuprates, the degeneracy of the p_x and p_y orbitals is already lifted at each O site due to its local twofold symmetry, being bonded to two neighboring Cu atoms. The modulating pattern of O $2p_x$ and $2p_y$ orbitals is also likely driven by their hybridization to localized Cu $3dx^2-y^2$ orbitals with strong electronic correlations (32). In $RSb\text{Te}$, the degeneracy of the p_x and p_y orbitals is preserved at each Sb site, which is bonded to four neighboring Sb atoms. The Sb square lattice here also represents a purer p -electron system, where the orbital texture is likely determined by interactions involving only p_x and p_y orbitals. It remains to be clarified whether the striking similarities between the CDW of $RSb\text{Te}$ and the charge order of cuprates are simply coincidental, or reflect some generic microscopic physics of p orbitals.

In conclusion, we have utilized STM to reveal the p -orbital texture within the 1×7 CDW state of nonstoichiometric $\text{Ce}(\text{Sb}_{1-x}\text{Te}_x)\text{Te}_{1-\delta}$. As future steps, it would be interesting to investigate the evolution of this orbital texture as the CDW wavelength changes across a wider doping range x , or the effects of uniaxial strain. In addition, it would be interesting to clarify whether this orbital texture has hidden orbital angular momentum, similar to that suggested by Raman spectroscopy for GdTe_3 and LaTe_3 (17), and if so, whether the orbital angular momentum and resulting orbital texture can be modified by flipping the Ce^{3+} moments with an external magnetic field.

Methods

Experimental

Single crystals of $\text{Ce}(\text{Sb}_{1-x}\text{Te}_x)\text{Te}_{1-\delta}$ were grown with iodine vapor transport, as described in Ref. (21). Magnetotransport measurements were performed with a physical property measurement system (PPMS) from Quantum Design using the standard four-probe method. The magnetic field was applied along the c axis while the current flowed in the a - b plane. We conducted STM experiments using a home-built, low-temperature, ultrahigh vacuum (UHV) instrument. The sample was cleaved in UHV on a cleaving stage cooled by liquid nitrogen, then quickly transferred to the microscope head held at 4.2 K. The topographic images were acquired in the constant-current mode. Unless otherwise indicated, the only processing performed on the topographic images shown in the manuscript (Figs. 2a, 2d, 3a, 3b, 3e, 3f, and 4c) were a background plane subtraction, or a row-by-row parabolic subtraction. Differential conductance spectra were obtained with the standard lock-in amplifier technique. We used a root-mean-square oscillation voltage between 1.4 and 20 meV and a lock-in frequency of 973 Hz.

To obtain the topographies at -0.5 and $+1.0$ V in Figs. 3a and 3b over the same area, with each pixel matched at the same position, we used the Multi Pass module of the Nanonis SPM Controller software. The Multi Pass mode enables each line of an image to be scanned multiple times using different parameters. Using a current setpoint of 20 pA, we scanned each line three times, with bias voltages of -0.5 , $+1.0$, and -0.5 V, respectively. The first two images are shown in Figs. 3a and 3b, while the third image served as a control to ensure minimal drift during the repeated scans of each line (see Supplementary Note 7).

Data analysis

We describe our analysis algorithms in greater detail:

Detecting positions of local maxima

1. Image parameters: 20×20 nm, 1216×1216 pixels.
2. Pre-processing (only for the purpose of detecting local maxima): For the topographic images (Figs. 3a and 3b), we applied 2D Gaussian smoothing of width σ ($=3$ pixels) and computed the 2D Laplacian to aid the detection of local maxima. For the Fourier-filtered images (Figs. 4a and 5a), the images were smooth enough to skip this step.
3. We defined a grid over the image with spacing n ($=2$ pixels). At every intersection point of the grid, we defined an $m \times m$ window ($m=16$ pixels) centered about this point and extracted the coordinates of the image maximum within this window. This procedure could identify all the local maxima corresponding to the atomic-sized lobes, but greatly overcounted the number of actual local maxima.
4. We removed every local maximum that lies within a threshold distance t ($=16$ pixels) of another local maximum. This removed duplicate points.

5. We removed every local maximum that lies on the boundary of the image.

Computing lobe anisotropy

1. Pre-processing (only for the purpose of computing lobe anisotropy): We applied 2D Gaussian smoothing of width σ ($=3$ pixels) to the topographic image in Fig. 3b.
2. We computed the second partial x and y derivatives at every pixel of the image.
3. At the coordinates (x_i, y_i) of every local maximum, we computed the anisotropy $\eta(x_i, y_i)$ as defined in Eq. (1).

Distribution of positions of anisotropic lobes within CeSbTe unit cell

1. We identified the set of coordinates $\{(x_i^-, y_i^-)\}$ of the local maxima in the Fourier-filtered -0.5 V topography, i.e., the positions of the Te atoms.
2. We identified the set of coordinates $\{(x_i^+, y_i^+)\}$ of the local maxima in the (Fourier-filtered) $+1.0$ V topography, i.e., the positions of the x - and y -anisotropic lobes.
3. For each anisotropic lobe at (x_i^+, y_i^+) , we identified the Te atomic position (x_j^-, y_j^-) that lies closest to (x_i^+, y_i^+) .
4. We computed the difference vector $(\Delta x_i, \Delta y_i) = (x_i^+ - x_j^-, y_i^+ - y_j^-)$.
5. We constructed 2D histograms of the difference vectors $(\Delta x_i, \Delta y_i)$, which represent the distribution of anisotropic lobes within a Te-centered unit cell (Figs. 4f and 5c).

Red-blue binning of topography

1. For each pixel of the topography in Fig. 5a, we determined the nearest anisotropic lobe and classified the pixel with an x or y label according to the x or y orientation of that nearest anisotropic lobe.
2. For all the pixels labeled “ x ,” the topography is displayed according to a red-white color map, red being maximum and white being minimum.
3. For all the pixels labeled “ y ,” the topography is displayed according to a blue-white color map, blue being maximum and white being minimum.

DFT

We performed DFT calculations using the Vienna Ab initio Simulation Package (VASP) (33). Since our STM measurements probed the paramagnetic phase of CeSbTe, we performed nonmagnetic calculations. We used the Perdew-Burke-Ernzerhof (PBE) parametrization of the generalized gradient

approximation (GGA) functional (34). We treated the Ce $5s^25p^66s^25d^1$, Sb $5s^25p^3$, and Te $5s^25p^4$ electrons as valence. The occupied Ce $4f^1$ electron was frozen in the core, since angle-resolved photoemission spectroscopy detected the $4f$ band to lie 3.1 eV below the E_F (21), which is beyond the energy range of our STM measurements. The energy cutoff for the plane-wave basis was 450 eV.

We computed the band structure (Fig. 1h), Fermi surface (Fig. 1i), and DOS (Fig. 3g) of $\text{Ce}(\text{Sb}_{1-x}\text{Te}_x)\text{Te}$ with $x = 0.37$ as follows: Using the virtual crystal approximation, we replaced Sb atoms in the Sb square lattice with fictitious atoms whose pseudopotential was a weighted average of 63% of the Sb pseudopotential and 37% of the Te pseudopotential (35). We adopted an orthorhombic $1 \times 1 \times 1$ unit cell with experimental lattice constants refined from powder x-ray diffraction (22): $a = 4.38895(6)$ Å, $b = 4.43760(7)$ Å, and $c = 9.33984(10)$ Å. The internal atomic coordinates were determined by structural optimization with a force tolerance of 5 meV/Å. We computed the DOS using a Brillouin zone sampling of $30 \times 30 \times 14$. For the Fermi surface, a different sampling of $32 \times 32 \times 16$ was used. For the band structure, spin-orbit coupling was incorporated in a non-self-consistent cycle.

For the partial charge densities shown in Fig. 3h, we constructed a $1 \times 1 \times 5$ slab of $\text{CeSb}_{0.63}\text{Te}_{1.37}$ with both surfaces terminated by a Te plane, again using the virtual crystal approximation to simulate the doping. We fixed the in-plane lattice constants to the same values of $a = 4.38895(6)$ Å and $b = 4.43760(7)$ Å, and used a c -axis size of 60 Å, which yielded a vacuum spacing of ~ 15 Å between periodic slabs. Internal atomic coordinates were relaxed with $12 \times 12 \times 1$ Brillouin zone sampling and a force tolerance of 10 meV/Å. A dipole correction was included to negate spurious interactions due to the slab asymmetry. After structural optimization, we calculated the wave function self-consistently with a Brillouin zone sampling of $44 \times 44 \times 1$, then computed the partial charge density integrated between 0 (= E_F) and -0.5 eV (left schematic of Fig. 3h), and between 0 and $+1.0$ eV (right schematic of Fig. 3h).

For the simulation of the 1×1 CDW state shown in Fig. 6a, we took as inspiration a $1 \times 1 \times 2$ CDW state proposed by Wang *et al.* (20) for nominally stoichiometric CeSbTe. In their proposed structure, each Sb layer form zigzag chains that uniformly extend along the a axis, and the zigzag chains in adjacent Sb layers are shifted along the b axis by half a unit cell. We constructed a $1 \times 1 \times 5$ slab of CeSbTe and fixed the in-plane lattice constants to the parameters refined by Wang *et al.*, $a = 4.3520(1)$ Å and $b = 4.3660(2)$ Å. We used a c -axis size of 60 Å, which yielded a vacuum spacing of ~ 15 Å between periodic slabs. By relaxing the internal atomic coordinates within VASP, we found that the Sb square lattices spontaneously formed zigzag chains along the a axis with phase shift of $b/2$ across adjacent Sb layers. We could reproduce the CDW pattern described by Wang *et al.*

We visualized crystal structures using VESTA (36) and Fermi surfaces using XCrySDen (37).

Acknowledgements

This project was funded by the Deutsche Forschungsgemeinschaft (DFG, German Research Foundation) – TRR 360 – 492547816. Sample growth was supported by the Gordon and Betty Moore Foundation's EPIQS initiative (grant number GBMF9064), by an NSF CAREER grant (DMR-2144295), and by the Air Force Office of Scientific Research under award number FA9550-20-1-0246. We thank M. Dueller and K. Pflaum for technical support and T.T.M. Palstra for useful discussions.

Contributions

X.Q. and Q.H performed the STM experiments under the supervision of L.Z. S.L. and L.S. synthesized the samples. X.Q., D.H., and H.T. analyzed and interpreted the data. D.H. performed the DFT calculations. X.Q. and D.H. prepared the manuscript with input from all co-authors.

References

1. E. DiMasi, B. Foran, M. C. Aronson, S. Lee, Stability of charge-density waves under continuous variation of band filling in $\text{LaTe}_{2-x}\text{Sb}_x$ ($0 \leq x \leq 1$). *Phys. Rev. B* **54**, 13587-13596 (1996).
2. H. Yao, J. A. Robertson, E. A. Kim, S. A. Kivelson, Theory of stripes in quasi-two-dimensional rare-earth tellurides. *Phys. Rev. B* **74**, 245126 (2006).
3. M. D. Johannes, I. I. Mazin, Fermi surface nesting and the origin of charge density waves in metals. *Phys. Rev. B* **77**, 165135 (2008).
4. Z. X. Zhang, X. P. Li, W. V. Liu, Stripe, checkerboard, and liquid-crystal ordering from anisotropic orbital Fermi surfaces in optical lattices. *Phys. Rev. A* **85**, 053606 (2012).
5. C. J. Wu, S. Das Sarma, $p_{x,y}$ -orbital counterpart of graphene: Cold atoms in the honeycomb optical lattice. *Phys. Rev. B* **77**, 235107 (2008).
6. C. J. Wu, Orbital ordering and frustration of band Mott insulators. *Phys. Rev. Lett.* **100**, 200406 (2008).
7. E. H. Zhao, W. V. Liu, Orbital order in Mott insulators of spinless p -band fermions. *Phys. Rev. Lett.* **100**, 160403 (2008).
8. X. P. Li, W. V. Liu, Physics of higher orbital bands in optical lattices: a review. *Rep. Prog. Phys.* **79**, 116401 (2016).
9. E. Dimasi, M. C. Aronson, J. F. Mansfield, B. Foran, S. Lee, Chemical Pressure and Charge-Density Waves in Rare-Earth Tritellurides. *Phys. Rev. B* **52**, 14516 (1995).
10. V. Brouet, W. L. Yang, X. J. Zhou, Z. Hussain, N. Ru, K. Y. Shin, I. R. Fisher, and Z. X. Shen, Fermi surface reconstruction in the CDW state of CeTe_3 observed by photoemission. *Phys. Rev. Lett.* **93**, 126405 (2004).
11. A. Fang, N. Ru, I. R. Fisher, A. Kapitulnik, STM studies of TbTe_3 : Evidence for a fully incommensurate charge density wave. *Phys. Rev. Lett.* **99**, 046401 (2007).
12. N. Ru, J.-H. Chu, I. R. Fisher, Magnetic properties of the charge density wave compounds $R\text{Te}_3$ ($R = \text{Y, La, Ce, Pr, Nd, Sm, Gd, Tb, Dy, Ho, Er, and Tm}$). *Phys. Rev. B* **78**, 012410 (2008).
13. A. Kogar, A. Zong, P. E. Dolgirev, X. Shen, J. Straquadine, Y.-Q. Bie, X. Wang, T. Rohwer, I.-C. Tung, Y. Yang, R. Li, J. Yang, S. Weathersby, S. Park, M. E. Kozina, E. J. Sie, H. Wen, P. Jarillo-Herrero, I. R. Fisher, X. Wang, N. Gedik, Light-induced charge density wave in LaTe_3 . *Nat. Phys.* **16**, 159 (2020).
14. J. A. W. Straquadine, M. S. Ikeda, I. R. Fisher, Evidence for Realignment of the Charge Density Wave State in ErTe_3 and TmTe_3 under Uniaxial Stress via Elastocaloric and Elastoresistivity Measurements. *Phys. Rev. X* **12**, 021046 (2022).
15. E. Lee, D. H. Kim, J. D. Denlinger, J. Kim, K. Kim, B. I. Min, B. H. Min, Y. S. Kwon, and J.-S. Kang, Angle-resolved and resonant photoemission spectroscopy study of the Fermi surface reconstruction in the charge density wave systems CeTe_2 and PrTe_2 . *Phys. Rev. B* **91**, 125137 (2015).
16. S. Lei, V. Duppel, J. M. Lippmann, J. Nuss, B. V. Lotsch, L. M. Schoop, Charge Density Waves and Magnetism in Topological Semimetal Candidates $\text{GdSb}_x\text{Te}_{2-x-\delta}$. *Adv. Quantum Technol.* **2**, 1900045 (2019).
17. Y. Wang, I. Petrides, G. McNamara, M. M. Hosen, S. Lei, Y.-C. Wu, J. L. Hart, H. Lv, J. Yan, D. Xiao, J. J. Cha, P. Narang, L. M. Schoop, K. S. Burch, Axial Higgs mode detected by quantum pathway interference in $R\text{Te}_3$. *Nature* **606**, 896 (2022).
18. C. Nayak, Density-wave states of nonzero angular momentum. *Phys. Rev. B* **62**, 4880 (2000).
19. S. Alekseev, S. A. A. Ghorashi, R. M. Fernandes, J. Cano, Charge density-waves with non-trivial orbital textures in rare earth tritellurides. arXiv:2404.17635v2.
20. Y. C. Wang, K. M. Poduska, R. Hoffmann, F. J. DiSalvo, Structure and physical properties of CeSbTe . *J. Alloy Compd.* **314**, 132 (2001).
21. L. M. Schoop, A. Topp, J. Lippmann, F. Orlandi, L. Muehler, M. G. Vergniory, Y. Sun, A. W. Rost, V. Duppel, M. Krivenkov, S. Sheoran, P. Manuel, A. Varykhalov, B. Yan, R. K. Kremer, C. R. Ast, B. V. Lotsch, Tunable Weyl and Dirac states in the nonsymmorphic compound CeSbTe . *Sci. Adv.* **4**, eaar2317 (2018).
22. R. Singha, T. H. Salters, S. M. L. Teicher, S. Lei, J. F. Khoury, N. P. Ong, L. M. Schoop, Evolving Devil's Staircase Magnetization from Tunable Charge Density Waves in Nonsymmorphic Dirac Semimetals. *Adv. Mater.* **33**, 2103476 (2021).

23. L. M. Schoop, M. N. Ali, C. Straer, A. Topp, A. Varykhalov, D. Marchenko, V. Duppel, S. S. P. Parkin, B. V. Lotsch, C. R. Ast, Dirac cone protected by non-symmorphic symmetry and three-dimensional Dirac line node in ZrSiS. *Nat Commun* **7**, 11696 (2016).
24. S. Klemenz, S. M. Lei, L. M. Schoop, Topological Semimetals in Square-Net Materials. *Annu. Rev. Mater. Res.* **49**, 185 (2019).
25. P. Li, B.J. Lv, Y. Fang, W. Guo, Z.Z. Wu, Y. Wu, D.W. Shen, Y.F. Nie, L. Petaccia, C. Cao, Z.-A. Xu, Y. Liu, Charge density wave and weak Kondo effect in a Dirac semimetal CeSbTe. *Sci. China Phys. Mech.* **64**, 237412 (2021).
26. T. Salters, F. Orlandi, T. Berry, J. F. Khoury, E. Whittaker, P. Manuel, and L. M. Schoop, Charge density wave-templated spin cycloid in topological semimetal NdSb_xTe_{2-x-δ}. *Phys Rev Mater* **7**, 044203 (2023).
27. T. Hanaguri, C. Lupien, Y. Kohsaka, D.-H. Lee, M. Azuma, M. Takano, H. Takagi, J. C. Davis, A ‘checkerboard’ electronic crystal state in lightly hole-doped Ca_{2-x}Na_xCuO₂Cl₂. *Nature* **430**, 1001 (2004).
28. Y. Kohsaka, C. Taylor, K. Fujita, A. Schmidt, C. Lupien, T. Hanaguri, M. Azuma, M. Takano, H. Eisaki, H. Takagi, S. Uchida, J. C. Davis, An Intrinsic Bond-Centered Electronic Glass with Unidirectional Domains in Underdoped Cuprates. *Science* **315**, 1380 (2007).
29. K. Fujita, M. H. Hamidian, S. D. Edkins, C. K. Kim, Y. Kohsaka, M. Azuma, M. Takano, H. Takagi, H. Eisaki, S.-i. Uchida, A. Allais, M. J. Lawler, E.-A. Kim, S. Sachdev, and J. C. S. Davis, Direct phase-sensitive identification of a *d*-form factor density wave in underdoped cuprates. *Proc. Natl. Acad. Sci.* **111**, E3026 (2014).
30. M. H. Hamidian, S. D. Edkins, Chung Koo Kim, J. C. Davis, A. P. Mackenzie, H. Eisaki, S. Uchida, M. J. Lawler, E.-A. Kim, S. Sachdev, K. Fujita, Atomic-scale electronic structure of the cuprate *d*-symmetry form factor density wave state. *Nat. Phys.* **12**, 150 (2016).
31. R. Comin, R. Sutarto, F. He, E. H. da Silva Neto, L. Chauviere, A. Fraño, R. Liang, W. N. Hardy, D. A. Bonn, Y. Yoshida, H. Eisaki, A. J. Achkar, D. G. Hawthorn, B. Keimer, G. A. Sawatzky, A. Damascelli, Symmetry of charge order in cuprates. *Nat. Mater.* **14**, 796 (2015).
32. M. Tsuchiizu, Y. Yamakawa, H. Kontani, *p*-orbital density wave with *d* symmetry in high-*T_c* cuprate superconductors predicted by renormalization-group + constrained RPA theory. *Phys. Rev. B* **93**, 155148 (2016).
33. G. Kresse and J. Furthmüller, Efficient iterative schemes for *ab initio* total-energy calculations using a plane-wave basis set. *Phys. Rev. B* **54**, 11169 (1996).
34. J. P. Perdew, K. Burke, M. Ernzerhof, Generalized Gradient Approximation Made Simple. *Phys. Rev. Lett.* **77**, 3865 (1996).
35. L. Bellaiche and D. Vanderbilt, Virtual crystal approximation revisited: Application to dielectric and piezoelectric properties of perovskites. *Phys. Rev. B* **61**, 7877 (2000).
36. K. Momma and F. Izumi, *VESTA 3* for three-dimensional visualization of crystal, volumetric and morphology data. *J. Appl. Cryst.* **44**, 1272-1276 (2011).
37. A. Kokalj, Computer graphics and graphical user interfaces as tools in simulations of matter at the atomic scale. *Computational Material Science*, **28**, 2 (2003).